Korean J. Chem. Eng., 39(7), 1775-1787 (2022)
DOI: 10.1007/s11814-022-1137-9

pISSN: 0256-1115
eISSN: 1975-7220

Carbon aerogel from waste corrugated cardboard: Facile preparation, characterization, and application to solar steam generation and adsorption

Yuhui Ma[*,**,†]

*The Institute of Seawater Desalination and Multipurpose Utilization (ISDMU), Ministry of Natural Resources
of the People's Republic of China, Tianjin 300192, China
**Tianjin Haiyue Water Treatment High-tech Co., Ltd, Tianjin 300192, China

(*Received 15 October 2021 • Revised 17 March 2022 • Accepted 2 April 2022*)

Abstract−Carbon aerogel ($CA_{Sol\text{-}Ads}$) was prepared from waste corrugated cardboard (WCC) by using a green and facile strategy and it was explored as an all-in-one solar evaporator and a floatable absorbent. Thermal conversion of carbon precursor was investigated using thermogravimetric analyzer coupled with Fourier transform infrared spectrometer. The amorphous carbon aerogel was made up of criss-crossing carbon ribbons and it had a typical micro-mesoporous structure and a specific surface area of 575 $m^2\ g^{-1}$. It exhibited remarkable optical absorption over 81.8% in the UV and Vis regions and over 70% in the NIR region. The surface temperature of dry $CA_{Sol\text{-}Ads}$ can achieve 77.9 °C under 1 kW m^{-2} irradiation. The hydrophilic 3D network structure of $CA_{Sol\text{-}Ads}$ provides a large volume for the storage of liquids; thus, the carbon aerogel was able to store as much as 13.4 times its own weight in water. Solar-driven evaporation rate over $CA_{Sol\text{-}Ads}$ saturated with water was calculated to be 1.68 kg $m^{-2}\ h^{-1}$, which was 4.5 times the value achieved with bare water under 1 kW m^{-2} irradiation. The adsorption behavior of $CA_{Sol\text{-}Ads}$ for methylene blue (MB) fitted the Langmuir isotherm model with the maximum monolayer adsorption capacity of 108 mg g^{-1}. The monolithic $CA_{Sol\text{-}Ads}$ can be used as a self-floating absorbent for the adsorption of MB from water, and the adsorption kinetics followed pseudo-second-order kinetics model.

Keywords: Waste Corrugated Cardboard, Carbon Aerogel, TG-FTIR, Photothermal Conversion, Solar Steam Generation, Floatable Adsorbent

INTRODUCTION

Carbon aerogels (CAs) are a class of synthetic carbon nanomaterials with interconnected three-dimensional (3D) networks [1]. CAs have gained extensive attention for their chemical stability, large surface area, excellent electrical conductivity, high porosity and low mass density [2]. Due to these excellent properties, CAs have been used for hydrogen storage, supercapacitors, catalysis, microwave adsorption, environmental purification, and so on [3,4].

Solar steam generation (SSG), which harvests solar energy to generate heat for evaporating water, is emerging as a quite promising approach for seawater desalination and wastewater purification because it avoids volumetric heating and uses the abundant and renewable solar energy as the only energy source [5,6]. The photothermal material is the most essential part of a given SSG system [7]. Recently, CAs have been greatly taken into consideration as photothermal materials for SSG systems. This is because CAs inherently absorb light through the photoexcitation of π electron in sp^2-hybridized carbon atoms, generating heat when the excited electron relaxes back to its ground state, and high porosity of CAs favors light-matter interactions inside the pores, as well as the increase of light absorption [8,9]. Fu et al. used graphene oxide as raw material to produce CA with evaporation rate higher than 2.50 kg $m^{-2}\ h^{-1}$ under 3 kW m^{-2} irradiation during SSG [10]. Deng et al. also used graphene oxide to prepared superwetting nitrogen-doped CA, and the evaporation rate of CA reached 1.41 kg $m^{-2}\ h^{-1}$ under 1 kW m^{-2} irradiation [11]. CA, with hierarchically porous structure, can be obtained from resorcinol-formaldehyde aerogel, and the product exhibited an evaporation rate of 1.29 kg $m^{-2}\ h^{-1}$ under 1 kW m^{-2} illumination [4]. CA was prepared by Mu et al. using tubular conjugated microporous polymer aerogel as precursor, and the product showed and evaporation rate of 1.44 kg $m^{-2}\ h^{-1}$ under 1 kW m^{-2} illumination [7].

Adsorption is a process during which adsorbates are fixed to the surface of solid adsorbents via physical or chemical interactions, and it is also considered to be one of the most promising methods in wastewater treatment owing to its simple operation, high removal efficiency, simplicity of design, and recyclability [12]. The quality of adsorbent is the key factor for the adsorption process [13]. In recent years, CAs have attracted much attention as adsorbents due to their high specific surface area and many accessible pores. Wang reported the preparation of carbon nanotube/graphene hybrid aerogel for the adsorption of a variety of organics and oils from water [14]. Porous nitrogen-doped magnetic CA was fabricated using melamine-formaldehyde as gel precursor and ferric nitrate as magnetic source and applied for the removal of organic dye Congo red [12]. Graphene/carbon nanotube aerogel was synthesized via hydrothermal treatment of graphene oxide and carbon nanotubes in ferrous ion solu-

---

[†] To whom correspondence should be addressed.
E-mail: myhbiomass@163.com

tion, and the product exhibited excellent adsorption ability to aqueous lead [15]. Nitrogen-doped activated mesoporous CA for the adsorption of methyl orange was obtained via carbonization and pickling using poly(vinyl alcohol) and chitosan as carbon sources and $AlCl_3 \cdot 6H_2O$ as both the solvent for chitosan and the hard template for porous structure [13].

For most of the previously reported fabrication processes of CAs, freeze-drying and/or supercritical drying are usually required to prevent the collapse of 3D network structures, resulting in the increased production costs. Moreover, graphene and carbon nanotube-based aerogel required expensive precursors, and CAs derived from polymers have the drawback of requiring toxic reagents and complicated production process. Therefore, it still remains a great challenge to explore the cost-effective and facile processes for the preparation of CAs.

In China, due to the rapid development of the express delivery industry, the number of corrugated cardboard boxes used as packaging materials achieved 40.6 billion in 2018, but the recovery rate of these packaging materials was less than one-tenth [16,17]. Presently, most of waste corrugated cardboard (WCC) is disposed of through landfill or incineration, so there is a strong motivation to develop sustainable and facile applications for WCC. WCC is mainly composed of cellulose, which is one of the most abundant and sustainable materials in nature [17,18]; therefore, it has high potential as an environmentally friendly precursor for carbon materials.

In the present study, a facile method was developed to convert WCC into a bifunctional CA. The main objectives of this study were to evaluate the potential of the WCC-derived CA as an all-in-one photothermal reservoir for SSG and an efficient floatable absorbent for water purification. The performance of a material depends on its physicochemical characteristics; thus, the product was analyzed by scanning electron microscope (SEM), N_2-adsorption/desorption, Fourier Transform infrared spectroscopy (FTIR), X-ray diffraction (XRD), Raman spectroscopy, and ultraviolet visible near infrared spectroscopy (UV-Vis-NIR). Moreover, in order to reveal the thermal conversion mechanism involved in the preparation process, the precursor was analyzed by a thermogravimetric analyzer coupled with Fourier transform infrared spectrometer (TG-FTIR).

EXPERIMENTAL

1. Preparation of Carbon Aerogel

WCC was first cut into 5 mm×5 mm sheets and sheared in an analytical mill (A11 basic, IKA, Germany) for 3 min. The sheared WCC (WCC_{She}) was mixed thoroughly with anhydrous ethanol under a ratio of 60 g : 1 L in a beaker, then the beaker was sealed and let stand at room temperature for 30 min. The mixture was poured into a glass tube with one end sealed by cellulose filter cloth for tricking filtration until no dripping ethanol could be observed. The wet WCC_{She} was then removed gently from the tubular glass mold, and dried in a fume hood for 2 h and let stand for another 12 h. The carbon precursor (denoted $WCC_{She\text{-}Et}$) with cylindrical shape could be obtained when the above steps were completed. $WCC_{She\text{-}Et}$ was then heated to 800 °C at a heating rate of 5 °C min^{-1} in N_2 atmosphere with the flow rate of 200 mL min^{-1} in a tube furnace (CTF12/65/550, Carbolite, Great Britain), and the final temperature was maintained for 2 h. Then the furnace was cooled to room temperature naturally to obtain the carbonized product. The carbonized product was soaked first with 1 M HCl several times and then washed with deionized water until the pH of the filtrate became constant, followed by drying at 105 °C for 6 h. Finally, carbon aerogel (denoted $CA_{Sol\text{-}Ads}$) was obtained. The yield of $CA_{Sol\text{-}Ads}$ was calculated as Yield (%)=(M_{CA}/M_{WCC})×100, where M_{CA} and M_{WCC} is the mass of the final product $CA_{Sol\text{-}Ads}$ and WCC used as raw material, respectively. The fabrication process of $CA_{Sol\text{-}Ads}$ is illustrated in Fig. 1. As shown, the carbonized product inherited the original cylindrical shape of $WCC_{She\text{-}Et}$ without any collapsing. The apparent density of $CA_{Sol\text{-}Ads}$ was calculated to be 61 mg cm^{-3} by dividing its mass (0.27 g) by the volume (4.396 cm^3). This low apparent density made $CA_{Sol\text{-}Ads}$ stand on a green bristlegrass. Moreover, the original macroscopic structure of $CA_{Sol\text{-}Ads}$ could be perfectly held even when it was pressed under two weights totaling 300 g, demonstrating that $CA_{Sol\text{-}Ads}$ had a good mechanical property because it was able to withstand the pressure of more than 1,100 times of its own weight.

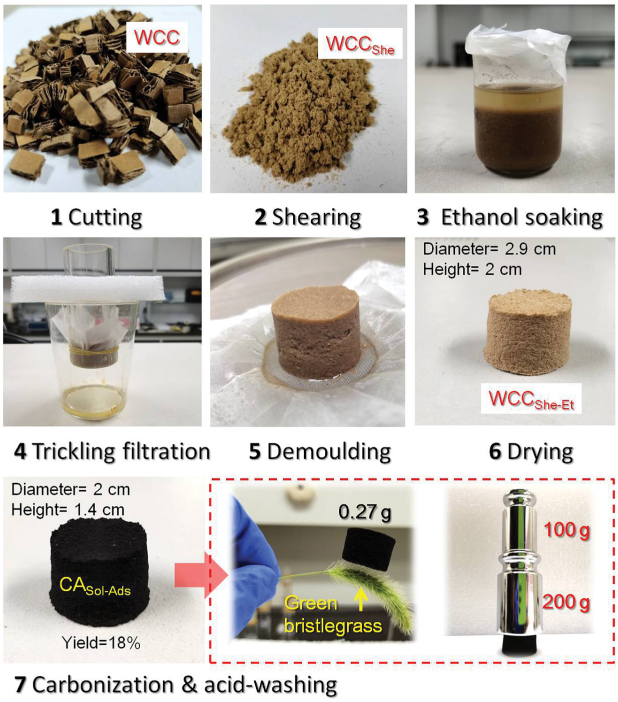

Fig. 1. Fabrication process of $CA_{Sol\text{-}Ads}$.

2. Characterization of Carbon Aerogel

Surface morphology was observed by using a scanning electron microscope (SEM) (Sigma 500, ZEISS, Germany). Physisorption analysis was carried out using a gas sorption analyzer (Autosorb-iQ, Quantachrome Instruments, USA) at –196 °C. BET surface area (S_{BET}) was calculated using Brunauer-Emmett-Teller (BET) method. Total pore volume (V_{Total}) was estimated from liquid volume of N_2 adsorbed at the saturation of relative pressure. Micropore volume (V_{Micro}) and the mesopore volume (V_{Meso}) were determined using the Horvath-Kawazo (HK) and Barret-Joyner-Halenda (BJH) methods, respectively. Average pore diameter (D_{Avg}) was calculated as

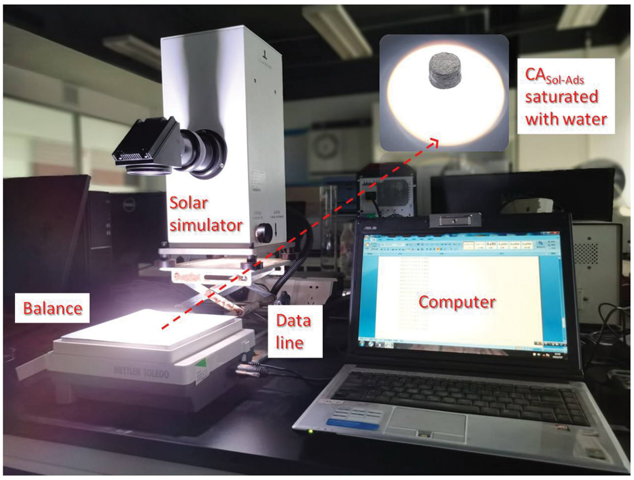

Fig. 2. Photograph of the solar steam generation setup.

$D_{Avg}=4V_{Total}/S_{BET}$. Density function theory (DFT) was used to calculate the pore size distribution from micropores to mesopores. Surface functional groups were detected using a Fourier transform infrared (FTIR) spectrometer (TENSOR II, Bruker, Germany). Crystal structure of was characterized using a X-ray diffractometer (XRD) (D8 ADVANCE, Bruker, Germany). Carbonaceous structure was analyzed by a Raman spectrometer (DXR, American Thermo Electron, USA). Optical absorption and reflection were studied using an ultraviolet-visible-near infrared (UV-Vis-NIR) spectrophotometer (Lambda 950, PerkinElmer, USA). Infrared images were taken by an infrared (IR) camera (TiS10, Fluke, USA), and the surface temperature of the sample was also measured using the IR camera.

3. Solar Steam Generation

A solar steam generation experiment was conducted at 25 °C and relative humidity of 30%. The experimental platform is illustrated in Fig. 2. $CA_{Sol-Ads}$ saturated with pure water was loaded on to an electronic balance (PL2002, Mettler-Toledo, Switzerland), which was connected to a computer to record mass change in real time. The irradiation with the solar intensity of 1 kW m^{-2} (1 sun) was provided by a solar simulator (CEL-S500, Ceaulight, China) that shined a collimated beam light onto $CA_{Sol-Ads}$ vertically.

4. Adsorption Study

Equilibrium adsorption of MB onto $CA_{Sol-Ads}$ was carried out using a literature method [19]. $CA_{Sol-Ads}$ was first ground to 100 mesh, then 0.01 g $CA_{Sol-Ads}$ powder was added into in a set of Erlenmeyer flasks containing 20 mL MB solutions with various initial concentrations (20, 30, 40, 50, 60 mg L^{-1}). The flasks were sealed using parafilm and agitated at 150 rpm and 30 °C for 72 h to reach equilibrium, then the suspensions were filtered by 0.45 μm membrane filters and the filtrates were diluted to suitable concentrations. MB concentration of the filtrates was analyzed using an UV-Vis spectrophotometer (DR5000, HACH, USA) at the maximum wavelength (λ) of 664 nm. MB uptake per unit mass of adsorbent at equilibrium, q_e (mg g^{-1}), was calculated by

$$q_e=\frac{C_0-C_e}{M}V \tag{1}$$

where C_0 and C_e (mg L^{-1}) are the initial and equilibrium liquid-phase concentrations of MB. V (L) is the volume of the solution and M (g) is the mass of $CA_{Sol-Ads}$ powder used. The equilibrium data were linearly fitted by Langmuir, Freundlich and Temkin isotherm models, which are expressed in Eq. (2), (3) and (4), respectively:

$$C_e/q_e=C_e/q_m+1/(K_Lq_m) \tag{2}$$

$$\log q_e=\log K_F+(1/n)\log C_e \tag{3}$$

$$q_e=(RT/b)\ln A_T+(RT/b)\ln C_e \tag{4}$$

where q_m (mg g^{-1}) is the maximum monolayer adsorption capacity of the sorbent, K_L (L mg^{-1}) is the Langmuir constant related to the free energy or net enthalpy of adsorption. K_F (mg g^{-1}) (L mg^{-1})$^{1/n}$ is Freundlich adsorption constant, indicating the relative adsorption capacity of the adsorbent, n is the heterogeneity factor. B_T= RT/b, with b (J mol^{-1}), A_T (L g^{-1}), R (8.314 J mol^{-1} K^{-1}) and T (K) are the Temkin constant related to heat of sorption, equilibrium binding constant, gas constant and absolute temperature, respectively [20,21].

The adsorption of MB by floating $CA_{Sol-Ads}$ in monolith form was performed in a beaker containing unbroken $CA_{Sol-Ads}$ and 100 mL of 10 mg L^{-1} MB solution. The beaker was sealed using parafilm and left undisturbed at room temperature. MB solution was sampled at certain time points by using a pipette and the concentration was measured using the UV-Vis spectrophotometer. After measurement, the MB solution extracted was returned into the beaker for further adsorption. Based on the above experimental data, the adsorption kinetics were analyzed by using pseudo-first-order, pseudo-second-order and Elovich kinetic models, which are expressed in Eq. (5), (6) and (7), respectively:

$$\ln(q_e-q_t)=\ln q_e-k_1t \tag{5}$$

$$t/q_t=1/(k_2q_e^2)+t/q_e \tag{6}$$

$$q_t=\frac{1}{\beta}\ln(\alpha\beta)+\frac{1}{\beta}\ln t \tag{7}$$

where q_e and q_t are the adsorption capacity (mg g^{-1}) at equilibrium time and at the time of t (min), respectively; k_1 (min^{-1}) and k_2 (g mg^{-1} min^{-1}) are the pseudo-first- and pseudo-second-order rate constants. α (g (mg min)$^{-1}$) and β (mg g^{-1}) are the initial adsorption rate constant and desorption constant of the Elovich model, respectively [22,23].

5. TG-FTIR Analysis

Weight loss and volatiles formed during the thermal conversion processes of WCC_{She} and WCC_{She-Et} were studied using a simultaneous thermal analyzer (STA 2500 Regulus, NETZSCH, Germany) coupled with a Fourier transform infrared spectrometer (TENSOR II, Bruker, Germany) (TG-FTIR). Each sample was heated from 35 to 900 °C with the heating rate of 20 °C min^{-1} and under N_2 with a flowing rate of 70 mL min^{-1}. The gaseous products were detected in real time by FTIR, and the spectra were recorded at wavenumber of 4,000 to 650 cm^{-1}. The transfer pipe and the sample cell in the FTIR system were heated at 200 °C to minimize secondary reactions.

6. Pyrolysis Kinetic Study

The data obtained from TG analysis of WCC_{She-Et} were used to determine its pyrolysis kinetics using Coats-Redfern equation [24,25].

The rate of conversion, $d\alpha/dt$, is a linear function of rate constant (k) and function of conversion, $f(\alpha)$:

$$\frac{d\alpha}{dt}=kf(\alpha) \tag{8}$$

Conversion degree (α) can be expressed as

$$\alpha=(m_i-m_t)/(m_i-m_\infty) \tag{9}$$

where t is reaction time. m_i, m_t and m_∞ are the initial mass of the sample, the mass of the sample at time t, and the final mass of the sample, respectively.

According to the Arrhenius law, the rate constant, k can be expressed as

$$k=A\exp(-E_a/RT) \tag{10}$$

where A is the pre-exponential factor, E_a is the activation energy, R is the gas constant, and T is the absolute temperature.

For a constant heating rate β, β=dT/dt, rearranging Eq. (10) and integrating by using Coats-Redfern method is given by

$$\ln[g(\alpha)/T^2]=\ln[AR/\beta E_a(1-2RT/E_a)]-E_a/RT \tag{11}$$

The term of $2RT/E_a$ is much less than 1, so it can be neglected, thus Eq. (11) is simplified as

$$\ln[g(\alpha)/T^2]=\ln(AR/\beta E_a)-E_a/RT \tag{12}$$

Depending on the different reaction models, it is possible to obtain a plot of $\ln[g(\alpha)/T^2]$ versus 1/T using the $g(\alpha)$ values listed in Table 1 [26,27]. E_a and A can be determined from the slope and the intercept of the plot, respectively.

Table 1. Expressions for the reaction mechanisms and its integrated form in solid state reactions

Reaction model	Symbol	$g(\alpha)$
Reaction order		
Zero order	F_0	α
First order	F_1	$-\ln(1-\alpha)$
Second order	F_2	$(1-\alpha)^{-1}-1$
Power law		
Power law, n=3/2	$P_{(2/3)}$	$\alpha^{3/2}$
Power law, n=1/2	P_2	$\alpha^{1/2}$
Power law, n=1/3	P_3	$\alpha^{1/3}$
Power law, n=1/4	P_4	$\alpha^{1/4}$
Nucleation and nuclei growth		
Avrami-Erofeev, n=1.5	$A_{1.5}$	$[-\ln(1-\alpha)]^{2/3}$
Avrami-Erofeev, n=2	A_2	$[-\ln(1-\alpha)]^{1/2}$
Avrami-Erofeev, n=3	A_3	$[-\ln(1-\alpha)]^{1/3}$
Avrami-Erofeev, n=4	A_4	$[-\ln(1-\alpha)]^{1/4}$
Phase boundary controlled reaction		
Contracting cylinder	R_2	$1-(1-\alpha)^{1/2}$
Contracting sphere	R_3	$1-(1-\alpha)^{1/3}$
Diffusion		
One-way transport	D_1	α^2
Two-way transport	D_2	$(1-\alpha)\ln(1-\alpha)+\alpha$
Three-way transport	D_3	$[1-(1-\alpha)^{1/3}]^2$
Ginstling-Brounshtein equation	D_4	$(1-2\alpha/3)-(1-\alpha)^{2/3}$

RESULTS AND DISCUSSION

1. TG-FTIR Analysis

1-1. Weight Loss Behavior

TG and derivative thermogravimetry (DTG) curves of WCC_{She} and $WCC_{She\text{-}Et}$ can be seen from Fig. 3. For WCC_{She}, the initial weight loss at low temperatures suggested the loss of moisture, and the major weight loss occurred within the temperature of 250-390 °C, with the maximum weight loss rate achieved at 367 °C, indicating the violent thermal cracking of cellulose in WCC. The weight loss rate of WCC_{She} became slow when the temperature exceeded 390 °C, indicating the complete thermal decomposition of cellulose and the occurrence of polymerization of carbonaceous structure of the newly formed char. The slight change in weight between 690 and 750 °C can be explained by the thermal degradation of inorganic components in the char. According to the TG and DTG curves of WCC_{She} and $WCC_{She\text{-}Et}$, there was almost no difference between their weight loss behaviors, suggesting that the anhydrous ethanol soaking process had no obvious effect on the chemical properties of WCC_{She}. Thus, there was no component of WCC_{She} released into anhydrous ethanol during soaking, and the anhydrous ethanol collected through trickling filtration after soaking of WCC_{She} contained no soluble impurity, so it can be readily reused after simple filtration.

1-2. Pyrolysis Kinetic

Pyrolysis kinetic parameters of $WCC_{She\text{-}Et}$ were determined by assuming single reaction mechanism for a particular thermal conversion stage. According to the weight loss regions of $WCC_{She\text{-}Et}$ (See Fig. 3), the main temperature range for pyrolysis reactions was selected. Eq. (12) was applied to the pyrolysis stage, and a series of straight lines were obtained by linear fitting $\ln[g(\alpha)/T^2)]$ versus 1/T (Fig. 4). The highest correlation coefficient (R^2) indicates that the

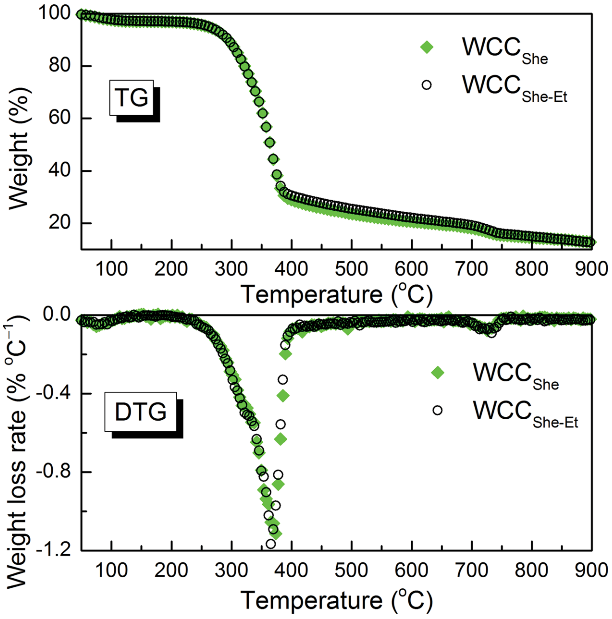

Fig. 3. TG and DTG curves of WCC_{She} and $WCC_{She\text{-}Et}$.

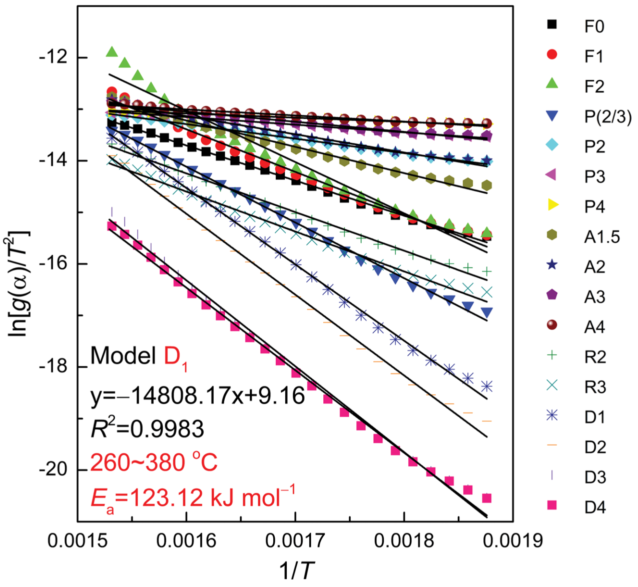

Fig. 4. Plots of ln[g(α)/T^2] versus 1/T for pyrolysis of WCC$_{She\text{-}Et}$ using different reaction models.

reaction model was the best fitted model for the experimental data. As shown, D_1 model showed the highest R^2 value achieved 0.9983, indicating that the transport of reactants or products from the site of chemical change was dominated by a diffusion process that was slower than the chemical steps. In addition, the activation energy of pyrolysis of WCC$_{She\text{-}Et}$ was calculated to be 123.12 kJ mol^{-1}.

1-3. Analysis of Gaseous Products

The volatiles evolved from the thermal conversion process of WCC$_{She\text{-}Et}$ were analyzed on-line by TG-FTIR. As shown in Fig. 5(a), the Gram-Schmidt curve reflects the variation of the yields of the gaseous products with temperature. A strong peak can be observed at 365 °C, suggesting the release of a large amount of volatile matters in a short period. There was a minor peak at 730 °C, which was due to the decomposition of the inorganic components of the char, resulting in the formation of a small amount of gaseous products. 3D (absorbance-wavenumber-temperature) spectra of the gaseous products released from WCC$_{She\text{-}Et}$ can be seen from the inset of Fig. 5(a). To analyze the gaseous products, absorbance information at different wavenumbers was obtained at a certain temperature. Fig. 5(b) shows the FTIR spectra at the peak temperatures of Gram-Schmidt curves of WCC$_{She\text{-}Et}$. Thermal cracking of cellulose at 365 °C led to the formation of a variety of molecules. The peaks at 3,742 and 1,508 cm^{-1} suggest the stretching vibrations of O-H in H_2O. The stretching vibration of C-H in aliphatic hydrocarbons resulted in the presence of the peak at 2,820 cm^{-1}. A strongest peak at 2,360 cm^{-1} indicates the presence of CO_2, and the two adjacent peaks at 2,188 and 2,100 cm^{-1} can be ascribed to CO. The absorption band of 1,750 cm^{-1} was ascribed to C=O stretching vibration of furfural [28]. The peak at 1,376 cm^{-1} was considered to be the aliphatic C-H stretching vibration [29]. The peak at 1,109 cm^{-1} suggests C-O-C stretching vibration of cyclic ether [30,31], indicating the presence of levoglucosan, a kind of anhydrosugar [32]. With the temperature increasing to 730 °C, CO_2 was observed as the only small molecule gaseous product. The evolution histories of gaseous products from WCC$_{She\text{-}Et}$ as a function of temperature are presented in Fig. 6. All the releasing curves exhibit sharp peaks at about 370 °C, indicating the thermal degradation of cellulose. CO_2 was the major gaseous product of cellulose pyrolysis, and it was generated via the cracking and reforming of carboxyl, carbonyl and ester groups [33]. Notably, CO_2 had an obvious peak at 730 °C, which can be attributed to the thermal decomposition of calcite ($CaCO_3$), a commonly used inorganic filler in paper products [16]. The release of furfural indicates that a large amount of ring-opening reactions occurred during the cellulose pyrolysis. H_2O was ascribed to cross-linking reactions between glucose molecules and dehydration within the pyran ring [32]. CO was formed via the decomposition of carbonyl groups via decarbonylation reactions [34].

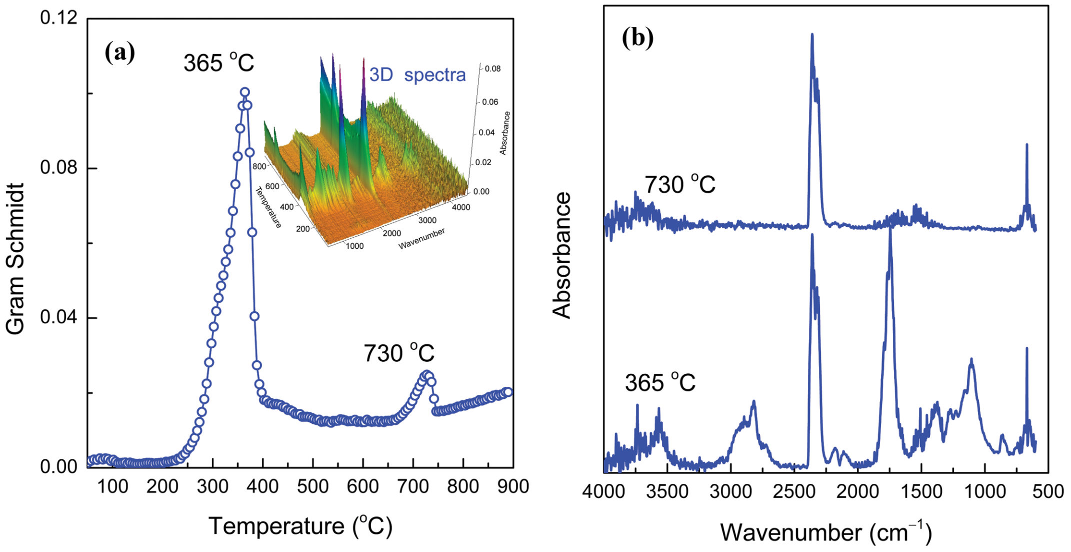

Fig. 5. (a) Gram-Schmidt curve of WCC$_{She\text{-}Et}$ and 3D spectra of volatiles produced from WCC$_{She\text{-}Et}$ (inset), and (b) FTIR spectra at the Gram-Schmidt peak temperatures for WCC$_{She\text{-}Et}$.

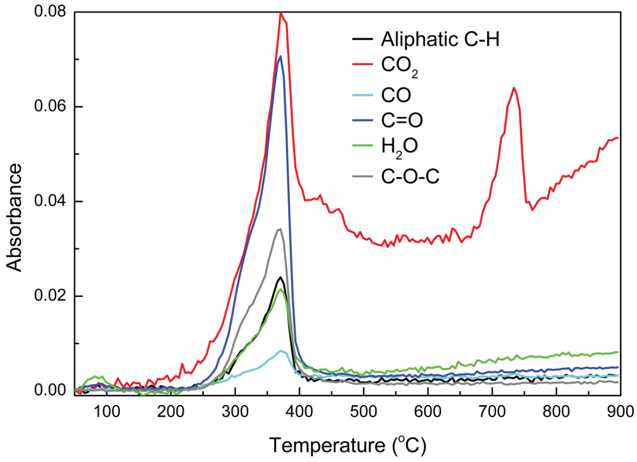

Fig. 6. Evolution history of gaseous products from $WCC_{She\text{-}Et}$ as a function of temperature.

2. Characterization of Sample

Fig. 7 shows photographs of WCC, $WCC_{She\text{-}Et}$, $CA_{Sol\text{-}Ads}$ and their SEM images under different magnification. As can be seen, the untreated WCC had a dense framework, which was made up of criss-crossed cellulose fibers. The fibers were ribbon-like, and the width of a single fiber was about 40 μm. $WCC_{She\text{-}Et}$ had a randomly oriented cellulose fibrous network structure, and the width of a single fiber decreased to 20 μm due to the mechanical force during grinding treatment. Unlike WCC, $WCC_{She\text{-}Et}$ had a loose structure with many spaces between the cellulose fibers. It is even more important to note that $WCC_{She\text{-}Et}$ underwent no structure collapse after drying, which was largely due to anhydrous ethanol that was used as the liquid phase. As known, the surface tension of ethanol is as low as 21.27 mN m^{-1}, which is much lower than that of water (71.96 mN m^{-1}). The surface tension of the evaporating solvent determines the capillary forces in micro-channels; thus, $WCC_{She\text{-}Et}$ exhibited perfect cylindrical-shaped appearance and loose microstructure

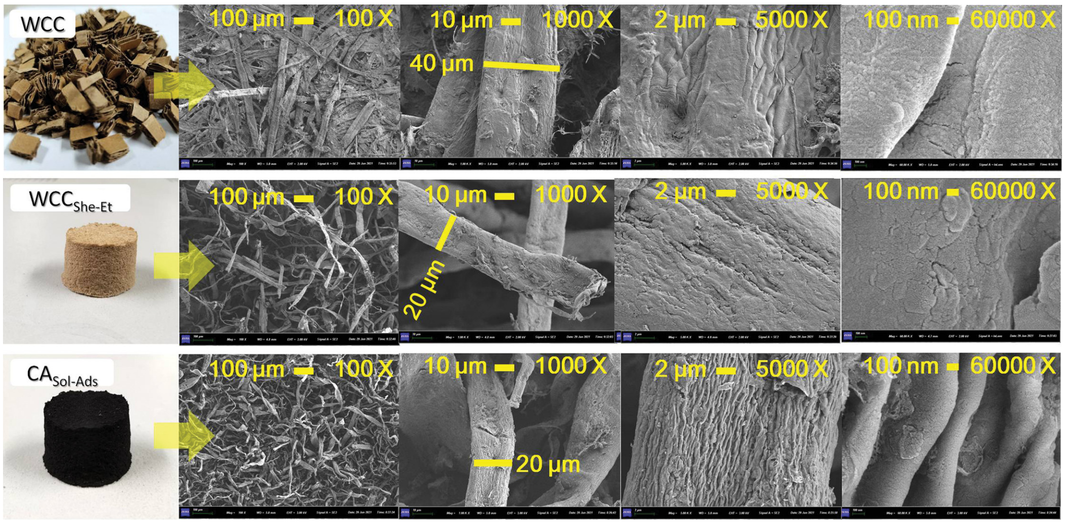

Fig. 7. Photographs of WCC, $WCC_{She\text{-}Et}$ and $CA_{Sol\text{-}Ads}$ and their SEM images under different magnification.

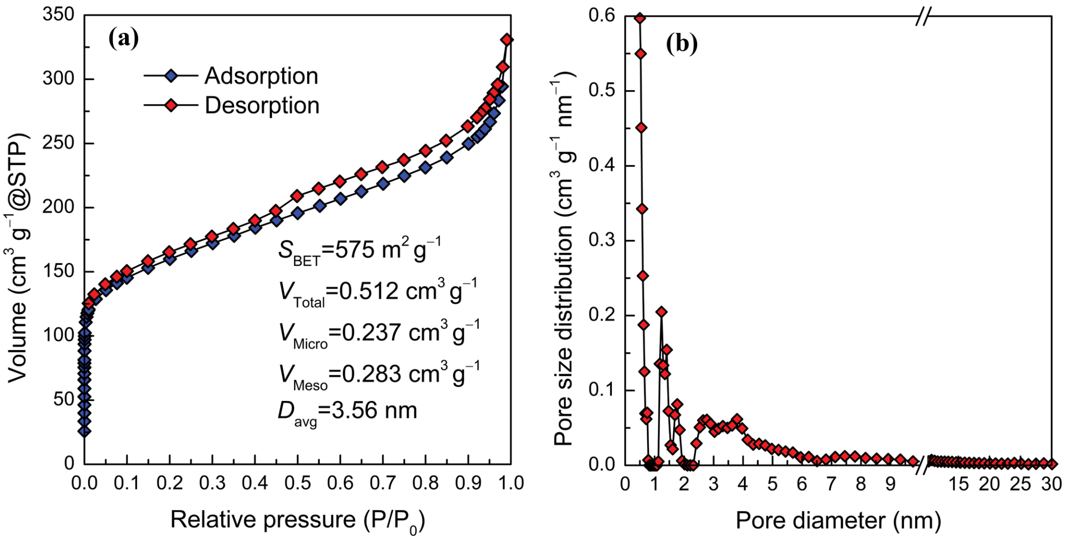

Fig. 8. (a) N_2-adsorption/desorption isotherms of $CA_{Sol\text{-}Ads}$ and (b) DFT pore size distribution curve of $CA_{Sol\text{-}Ads}$.

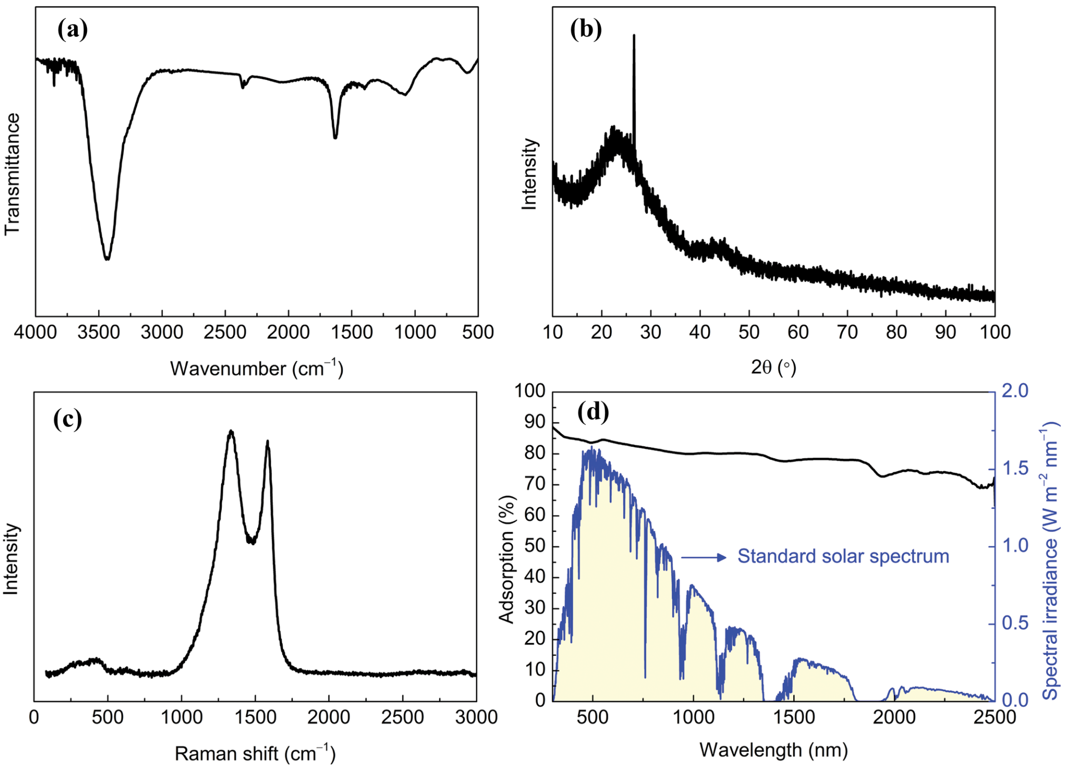

Fig. 9. (a) FTIR spectra, (b) XRD pattern, (c) Raman spectra and (d) UV-Vis-NIR spectra of CA$_{Sol-Ads}$.

due to the low surface tension of ethanol and its small capillary interaction with the fibers in WCC$_{She}$ during drying [35]. CA$_{Sol-Ads}$ had an irregular macroporous network structure inherited from WCC$_{She-Et}$, indicating that the carbonization process did not destroy the macroscopic structure of the precursor. Although carbonization had no obvious effect on the width of the ribbon-like fibers, the carbon fibers in CA$_{Sol-Ads}$ were more twisted and dense than the cellulose fibers in WCC$_{She-Et}$, and it is worth noting that there were many wrinkles and gullies on the rough surface of the carbon fibers.

Fig. 8(a) shows N_2-adsorption-desorption isotherms of CA$_{Sol-Ads}$. The product exhibits a combined type I and type IV adsorption isotherm with a maximum N_2 adsorption of 330.77 cm^3 g^{-1} when the relative pressure reached 0.9909. The uptake of N_2 within the low relative pressures ($P/P_0 \leq 0.01$) suggests the filling of micropores (diameter≤2 nm). The uptake at higher relative pressures (P/P_0= 0.40 to 0.9) and the hysteresis loop demonstrates the filling and emptying of mesopores (2 nm<diameter<50 nm) by capillary condensation. The sharp nitrogen uptake at high relative pressures ($P/P_0>0.9$) is related to the existence of large mesopores. The above results demonstrate the co-existence of micropores and mesopores in CA$_{Sol-Ads}$. Pore characteristic parameters including BET surface area (S_{BET}), total pore volume (V_{total}), micropore volume (V_{micro}), mesopore volume (V_{meso}), and average pore diameter (D_{avg}) of CA$_{Sol-Ads}$ can be seen from the inset. As shown, the ratio of V_{micro} and V_{meso} is 0.84; thus, CA$_{Sol-Ads}$ was considered as a typical micro-mesoporous carbon material. DFT pore size distribution curve of CA$_{Sol-Ads}$ is shown in Fig. 8(b). The curve has sharp peaks at 0.50 and 1.23 nm, suggesting the presence of micropores, and it also contains abundant mesopores with diameter ranging from 2.30 to 5.90 nm. The above results prove that CA$_{Sol-Ads}$ has a hierarchical porous structure, which is beneficial for its adsorption of organic molecules with different sizes [36,37].

FTIR spectra of CA$_{Sol-Ads}$ are shown in Fig. 9(a). The prominent broad peak at 3,442 cm^{-1} can be assigned to O-H groups bonded to aromatic rings [38]. The peak at 1,630 cm^{-1} was caused by C=O stretching conjugated with aromatic rings [39], and the subtle peak at 1,400 cm^{-1} indicates C-H in plane deformation combined with aromatic ring vibration [40]. The peak at 1,080 cm^{-1} corresponds to C-O and C-O-C stretching vibration [41,42].

Fig. 9(b) shows the XRD pattern of CA$_{Sol-Ads}$. As shown, the broad and low intensity peak centered at 23.19° correspond to the diffraction of (002) plane of the disordered graphite lattice, indicating the degree of orientation of aromatic carbon net in microcrystal [43]. The sharp peak at 26.55° is related with the (101) plane of quartz (SiO_2). As known, sodium silicate (Na_2SiO_3) is usually used as an adhesive in corrugated cardboard [44], and the presence of SiO_2 can be explained by the formation of H_2SiO_3 via the reaction between Na_2SiO_3 and HCl during the pickling process and the decomposition of H_2SiO_3 during the drying process.

Raman spectroscopy is widely used to characterize the structural features of carbon-containing materials. As shown in Fig. 9(c), the D band at 1,335 cm^{-1} in Raman spectra of CA$_{Sol-Ads}$ suggests disorder and indicates the presence of amorphous carbon, and it is also attributed to the in-plane defects and other disordered structures in graphite, while G band at 1,578 cm^{-1} suggests the vibration of sp^2-hybridized carbon atoms in the ideal two-dimensional hexagonal lattice [45]. The simultaneous presence of D and G bands suggests the heterogeneous carbon microstructure of $CA_{Sol\text{-}Ads}$. In addition, the disordered D peak exhibits a higher intensity than the graphite crystal G peak, suggesting a higher content of amorphous carbon in the sample.

High light adsorption is one of the key properties for an efficient photothermal material. UV-Vis-NIR spectroscopy can directly reflect the spectral absorption of materials. The absorption spectra of $CA_{Sol\text{-}Ads}$ are presented in Fig. 9(d). $CA_{Sol\text{-}Ads}$ exhibits light absorption over 70% across the entire spectrum range, and it was found to have high absorption over 81.8% in the UV and Vis regions (280-780 nm), indicating its potential to harvest solar energy for photothermal conversion. The excellent light absorption performance of $CA_{Sol\text{-}Ads}$ can be explained in three ways. First, the large delocalized π bonds in $CA_{Sol\text{-}Ads}$ can absorb almost every wavelength of the solar spectrum [46]. Second, $CA_{Sol\text{-}Ads}$ is made up of a complex 3D network of micrometer scale ribbon-like carbon fibers with nanometer scale wrinkles on their surfaces, and there are many microcavities between these carbon ribbons (See Fig. 7). So when the incident light encounters the carbon ribbons, it can be trapped by the fine hierarchical structures of $CA_{Sol\text{-}Ads}$ and bounces back and forth between the neighboring ribbons and the walls of the wrinkles, resulting in the enhanced light travelling distance, which facilitates light absorption [9,47,48]. Finally, $CA_{Sol\text{-}Ads}$ has a high S_{BET} of 575 $m^2\ g^{-1}$ and a micro-mesoporous structure. The results of previous studies have demonstrated that carbon aerogels composed of micropores could obviously decrease the reflection of visible light, because the vibration of electrons in carbon matrix can be limited by the interface of small-size pores, leading to the decrease in the reflection of visible light and increase in light absorption [4,49].

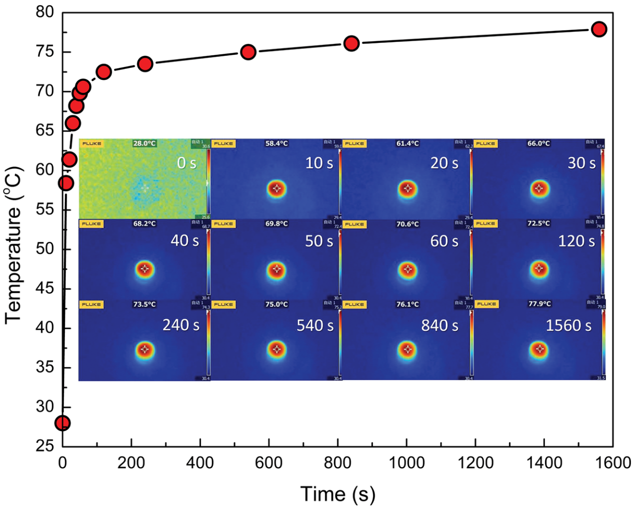

Fig. 10. Variation of the recorded temperature of upper surface of $CA_{Sol\text{-}Ads}$ in dry state with irradiation time; the inset shows IR images of dry $CA_{Sol\text{-}Ads}$ under 1 sun irradiation at various time points.

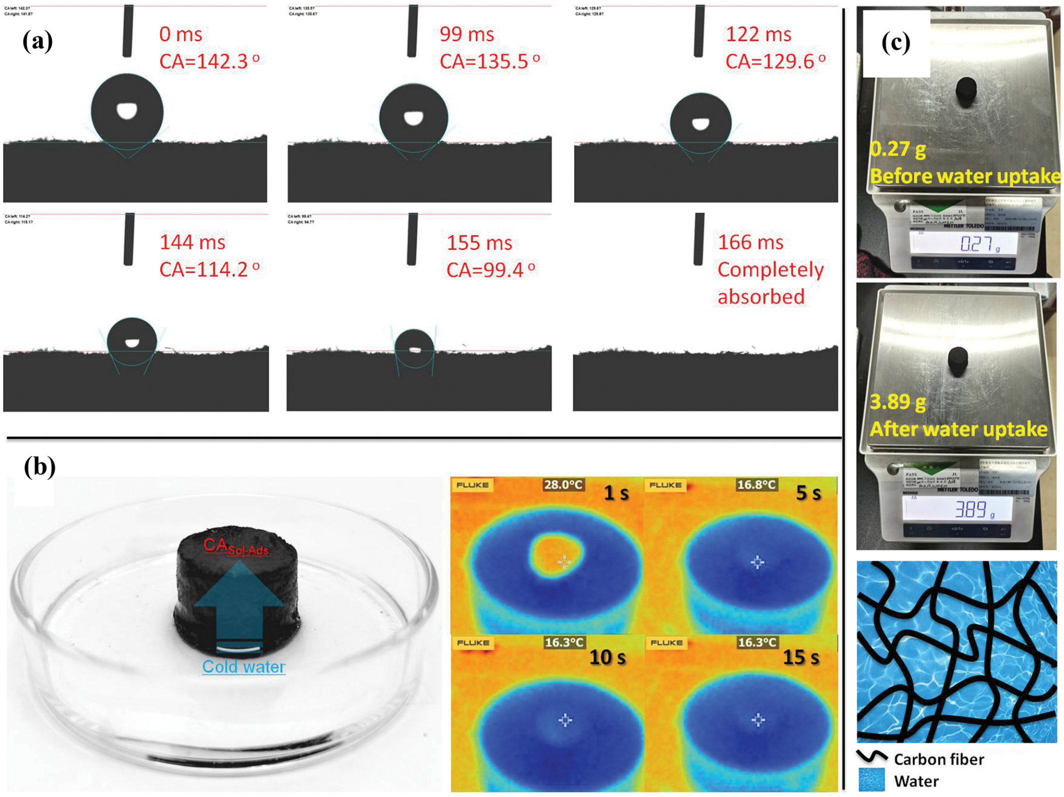

Fig. 11. (a) High-speed camera photos of the water droplet impregnation process on the surface of $CA_{Sol\text{-}Ads}$, (b) test of water pumping performance of $CA_{Sol\text{-}Ads}$ and IR images corresponding to different time after $CA_{Sol\text{-}Ads}$ was in touch with water, (c) photographic illustration of mass change of $CA_{Sol\text{-}Ads}$ before and after water uptake, and illustration of water stored in $CA_{Sol\text{-}Ads}$.

To evaluate the photothermal conversion performance of CA$_{Sol\text{-}Ads}$, it was irradiated by 1 sun (1 kW m^{-2}) simulated solar light in dry state under 25 °C and 30% relative humidity. The variation of the temperature of the upper surface of CA$_{Sol\text{-}Ads}$ can be seen from Fig. 10, and the inset shows the IR images of CA$_{Sol\text{-}Ads}$ at various time points. As shown, once the dry CA$_{Sol\text{-}Ads}$ is exposed to light, the upper surface temperature rises rapidly from 28 to 58.4 °C within the first 10 s, demonstrating its excellent photothermal conversion ability. The temperature eventually increases by 49.9 °C after 1,560 s and stabilizes at 77.9 °C. The results prove that solar energy can be effectively absorbed by CA$_{Sol\text{-}Ads}$ and transformed into heat; therefore, CA$_{Sol\text{-}Ads}$ has real potential to be a good candidate for SSG systems.

The water contact angle measurements were used to assess the hydrophilicity of CA$_{Sol\text{-}Ads}$. As depicted in Fig. 11(a), when water droplets come into contact with the surface of CA$_{Sol\text{-}Ads}$, both the contact angle and the volume of the droplet become steadily smaller, and the water droplet permeates completely into CA$_{Sol\text{-}Ads}$ within only 166 ms, indicating that CA$_{Sol\text{-}Ads}$ has excellent hydrophilicity. Furthermore, the water pumping performance of CA$_{Sol\text{-}Ads}$ was evaluated by a capillary water absorption experiment, and the rapid water diffusion through CA$_{Sol\text{-}Ads}$ can be seen from Fig. 11(b). According to IR images, the up surface temperature of CA$_{Sol\text{-}Ads}$ was 28 °C before being in touch with water. Once the bottom surface of CA$_{Sol\text{-}Ads}$ was in touch with water, the wetting process occurred rapidly due to water absorption and transportation. The up surface temperature of CA$_{Sol\text{-}Ads}$ reduced to 16.8 °C within only 5 s, because water of a lower temperature was pumped quickly from the bottom to the top of CA$_{Sol\text{-}Ads}$. The results indicate that CA$_{Sol\text{-}Ads}$ exhibits hydrophilic property as a monolithic material. Several previous studies have shown that carbon aerogel materials are usually hydrophobic due to the elimination of polar oxygen-containing functional groups by high temperature treatment and the intrinsic hydrophobic surface of graphitic carbon [50-55]. There are two reasons for the hydrophilicity of CA$_{Sol\text{-}Ads}$. First, there was SiO_2 in the carbon matrix of CA$_{Sol\text{-}Ads}$, and SiO_2 is a typical hydrophilic mineral due to the presence of hydroxyl groups (Si-OH) [56-58]. Second, CA$_{Sol\text{-}Ads}$ itself contained polar functional groups such as C=O, C-O and C-O-C. The fast water transport was largely due to the microscale cavities and channels in CA$_{Sol\text{-}Ads}$, which could be referred as the abundant capillary tubes [58]. Besides, water transport can also be strengthened by the hydrophilic surface. In addition, as shown in Fig. 11(c), CA$_{Sol\text{-}Ads}$ weighed only 0.27 g in dry state; however, when it absorbed water to its full capacity, the weight increased to 3.89 g, suggesting that up to 3.62 g of water was absorbed by CA$_{Sol\text{-}Ads}$. The result proves that CA$_{Sol\text{-}Ads}$ could absorb and securely retain as much as 13.4 times its own weight in water without visual shape distortion. As illustrated, the reason for the high water absorbency is that CA$_{Sol\text{-}Ads}$ had a developed porous network structure and a large pore volume; thus, water can be stored in the interconnected channels inside.

3. Application of Carbon Aerogel

3-1. Solar Steam Generation

Encouraged by the excellent photothermal property and water absorbency of CA$_{Sol\text{-}Ads}$, we further explored its application as an all-in-one SSG device without bulk water. In other words, CA$_{Sol\text{-}Ads}$ was not used solely as a photothermal material; it was also used as a water reservoir. This design can greatly simplify the SSG system because there is no need in the extra container filled with bulk water; thus, it would be a major advance in developing portable SSG device. Moreover, the risk of contaminating the produced clean water by raw water can be avoided. SSG over CA$_{Sol\text{-}Ads}$ saturated with pure water was tested under 25 °C and 30% relative humidity. Fig. 12 shows the IR images and the variation of temperature of the top surface of CA$_{Sol\text{-}Ads}$ under 1 sun irradiation at various time points. Upon solar irradiation, the top surface of CA$_{Sol\text{-}Ads}$ effectively absorbs the light and converts it into heat, resulting in an increase in temperature. As can be seen, the temperature of the top surface increased from 25.6 to 35.3 °C within 10 min, then slowly increased to 37.5 °C after 180 min. Note that the temperature of the side surface of CA$_{Sol\text{-}Ads}$ remained lower than the surrounding temperature, and this temperature deficit resulted in a net energy gain from the surrounding air, which was beneficial for

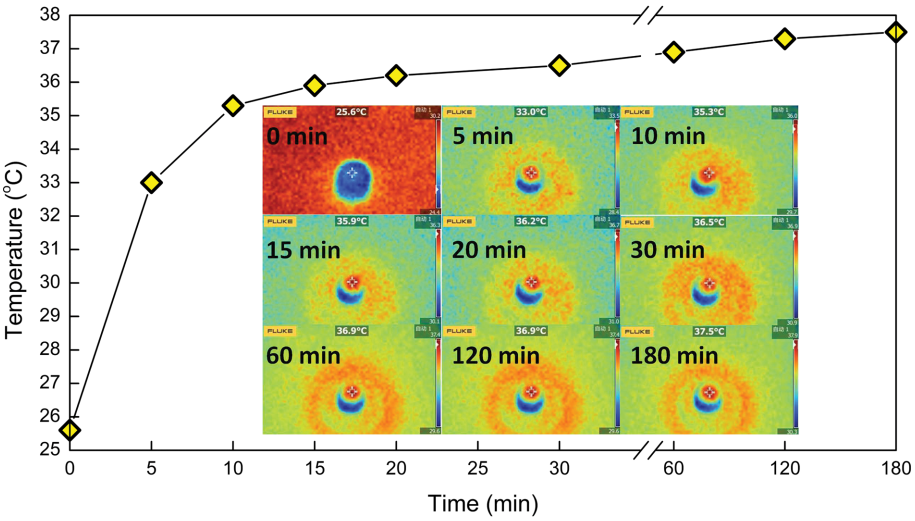

Fig. 12. Temperatures of the upper surface of CA$_{Sol\text{-}Ads}$ saturated with water under 1 sun irradiation at various time points, the inset shows IR images of CA$_{Sol\text{-}Ads}$ saturated with water under irradiation at various time points.

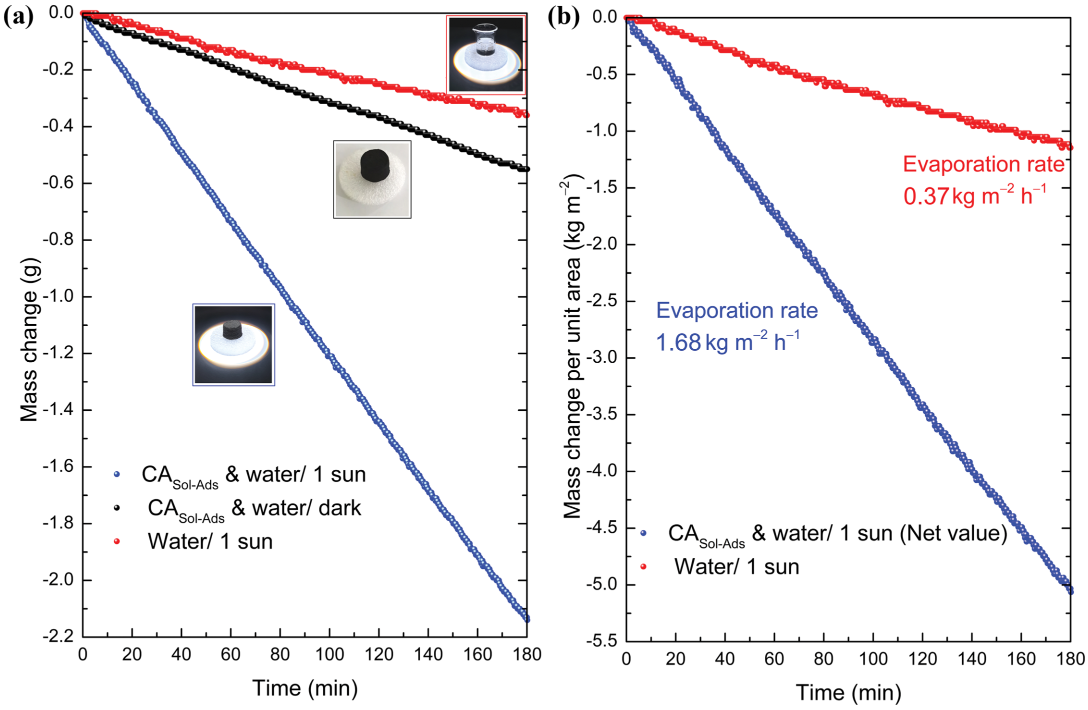

Fig. 13. (a) Mass change and (b) mass change per unit area of different evaporation systems at different time points.

Table 2. Water evaporation rates of solar evaporators based on different biomass-derived carbon materials under 1 sun irradiation

Raw material	Carbonization condition	Evaporation rate (kg m^{-2} h^{-1})	Ref.
Platanus fruits	180 °C/1 h, 600 °C/1 h	2.00	[59]
Coffee grounds	1,000 °C/1 h	1.05	[60]
Carp meat and bonemeal	500 °C/6 h	1.48	[61]
Lotus seedpod	500 °C/2 h	1.30	[62]
Tofu	300 °C/1 h, 600 °C/2 h	1.65	[63]
Carrot	550 °C/0.5 h	2.04	[64]
Mushroom	500 °C/12 h	1.48	[65]
WCC	800 °C/2 h	1.68	This study

the overall water evaporation of the SSG system.

Fig. 13(a) shows that when 3.62 g pure water contained in a 5 mL beaker (internal diameter 2 cm) was exposed to 1 sun irradiation for 180 min, the final mass change was 0.35 g, while the mass change of CA$_{Sol\text{-}Ads}$ saturated with 3.62 g pure water under 1 sun irradiation for 180 min achieved 2.17 g. Besides, water evaporation without light irradiation (dark evaporation) over CA$_{Sol\text{-}Ads}$ was 0.56 g after 180 min. As shown in Fig. 13(b), the net mass change (with dark evaporation subtracted) per unit area over CA$_{Sol\text{-}Ads}$ under 1 sun irradiation was calculated to be 5.03 kg m^{-2} based on its projected area, which was much higher than that of water contained in the beaker (1.11 kg m^{-2}), suggesting that the solar steam generation performance was dramatically improved by the effective photothermal conversion of CA$_{Sol\text{-}Ads}$. Moreover, the evaporation rate of water absorbed by CA$_{Sol\text{-}Ads}$ under 1 sun irradiation achieved as high as 1.68 kg m^{-2} h^{-1}. For comparison, the water evaporation rates of solar evaporators based on different biomass-derived carbon materials are listed in Table 2.

3-2. Adsorption of Methylene Blue

CA$_{Sol\text{-}Ads}$ has a high S_{BET} and many micro- and mesopores, allowing full access by adsorbate molecules, so it has real potential as an adsorbent. Equilibrium study of adsorption provides information on the capacity of the adsorbent, and the adsorption isotherm is important to describe how the adsorbate molecules are distributed between the liquid phase and solid phase when an adsorption system reaches equilibrium state. The adsorption isotherm of MB on CA$_{Sol\text{-}Ads}$ is shown in Fig. 14(a). MB adsorption capacity at equilibrium increased with the increasing initial concentration of MB, because higher concentration provided greater driving force for MB transferring from bulk water to CA$_{Sol\text{-}Ads}$ surface. The linear fitting of equilibrium data by Langmuir, Freundlich and Temkin isotherm models is shown in Fig. 14(b)-(d). The calculated constants of the three isotherm equations along with correlation coefficients (R^2) values are presented in Table 3. Langmuir model

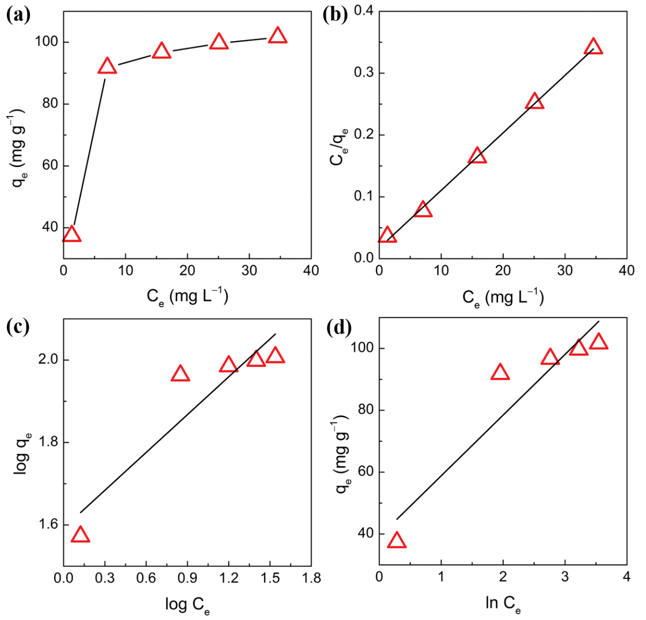

Fig. 14. (a) Adsorption isotherm of MB on powdered $CA_{Sol\text{-}Ads}$, linear fitting of equilibrium isotherm data by (b) Langmuir, (c) Freundlich and (d) Temkin isotherm models.

was best fitted with the equilibrium data due to its highest R^2 value. This model assumes uniform energy of adsorption onto the surface and no transmigration of the adsorbate in the plane of the surface. It describes monolayer adsorption onto a surface containing a finite number of identified sites. The conformation to Langmuir isotherm model suggests the formation of an MB monolayer on the outer surface of $CA_{Sol\text{-}Ads}$ and no further adsorption took place after the monolayer formation.

After determining the theoretical maximum MB adsorption capacity of $CA_{Sol\text{-}Ads}$, this material was further used as a floatable adsorbent for MB adsorption in the form of monolith. As known, the main advantage of the floating adsorption technology is that the adsorbents and contaminants can be enriched on the water surface and collected with the natural flow of water and easily separated from the water surface [21]. As depicted in the inset of Fig. 15(a), $CA_{Sol\text{-}Ads}$ was put into a beaker containing MB solution (100 mL, 10 mg L^{-1}) and left undisturbed for the simulation of the process of the purification of natural water using a floating absorbent. $CA_{Sol\text{-}Ads}$ achieved stable self-floating state on MB solution surface

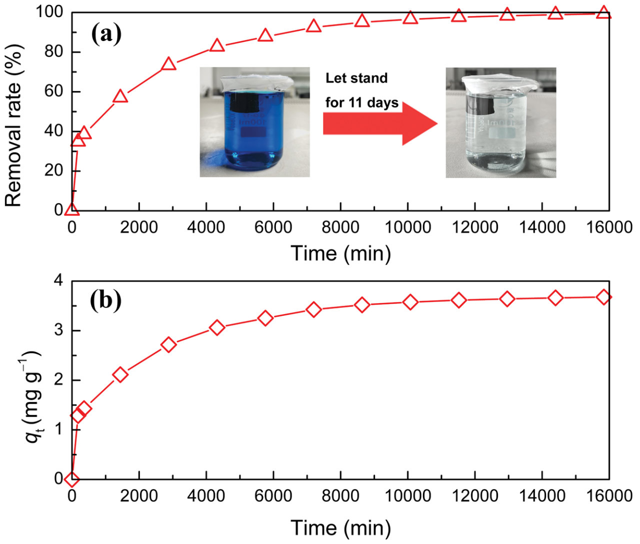

Fig. 15. (a) Effect of contact time on removal rate of MB by floating monolithic $CA_{Sol\text{-}Ads}$ and photographs of MB solution before and after adsorption (inset), (b) effect of contact time on MB uptake on floating monolithic $CA_{Sol\text{-}Ads}$.

Table 3. Fitting parameters for Langmuir, Freundlich and Temkin isotherm models

Langmuir			Freundlich			Temkin		
q_m	K_L	R^2	K_F	n	R^2	A_T	B_T	R^2
108	0.53	0.9984	39.13	3.27	0.8097	7.36	19.64	0.8519

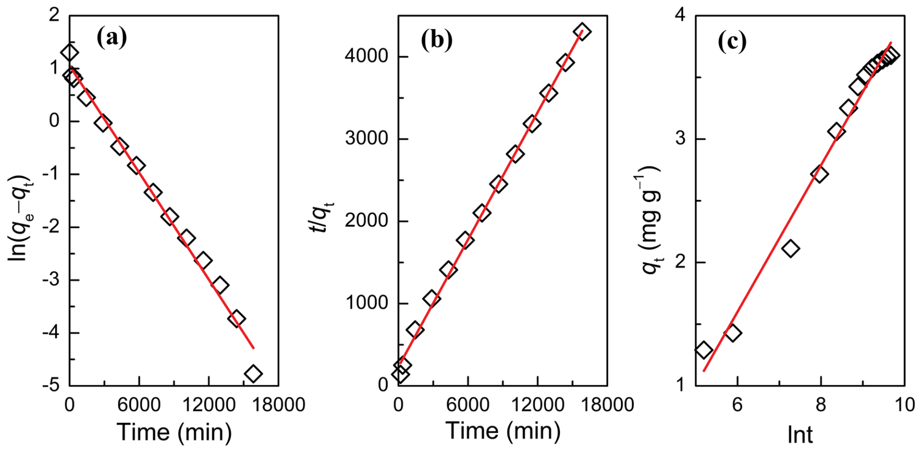

Fig. 16. (a) Pseudo-first-order, (b) pseudo-second-order, and (c) Elovich kinetics plot for the adsorption of MB by $CA_{Sol\text{-}Ads}$.

Table 4. Fitting parameters of pseudo-first-order, pseudo-second-order and Elovich kinetic models

$q_{e, exp}$	Pseudo-first-order			Pseudo-second-order			Elovich		
	k_1	$q_{e1, calc}$	R^2	k_2	$q_{e2, calc}$	R^2	α	β	R^2
3.69	3.37	2.87	0.9887	2.8×10^{-4}	3.86	0.9978	2.2×10^{-2}	1.68	0.9812

without external force, then the beaker was sealed using parafilm to prevent evaporation. $CA_{Sol\text{-}Ads}$ can quickly adsorb MB by more than 34% within the first 180 min, owing to the large number of active sites available for the adsorption. Prolonging the adsorption time, active sites were gradually occupied and inaccessible; thus, removal rate increased slowly but continually and finally reached more than 99% after 15,840 min (11 day). The inset also shows that the MB solution became colorless after standing for 11 days. Fig. 15(b) shows the variation of MB adsorption capacity of $CA_{Sol\text{-}Ads}$ with time, which displays the same varying tendency with the removal rate. These results prove that $CA_{Sol\text{-}Ads}$ with a monolithic appearance has a high potential as a floating adsorbent for the removal of dissolved contaminants from water environment in a practical application. In addition, the monolith character of $CA_{Sol\text{-}Ads}$ was perfectly retained after 11 days due to its good mechanical stability. Also, $CA_{Sol\text{-}Ads}$ still floated on the water surface after complete adsorption because of its low density, and this behavior allows one to easily collect this adsorbent after completing adsorption. Benefiting from its characteristics, we may find uses for $CA_{Sol\text{-}Ads}$ in purification of pond and landscape water, as well as treatment of oil spills. The linear fitting of experimental data by pseudo-first-order, pseudo-second-order and Elovich kinetics models is shown in Fig. 16(a)-(c), respectively, and the kinetics parameters for the adsorption of MB are summarized in Table 4. Based on the values of R^2, it can be concluded that the pseudo-second-order model is more suitable to represent the MB adsorption process onto $CA_{Sol\text{-}Ads}$, suggesting that the rate-limiting step of adsorption is a chemical interaction process involving valence forces via sharing and exchanging the electrons between MB and $CA_{Sol\text{-}Ads}$ [19,20].

CONCLUSION

Hierarchical porous carbon aerogel was successfully produced from waste corrugated cardboard by a procedure of shearing, ethanol soaking, drying, carbonization and pickling in turn. The carbon aerogel was suitable to be used as a photothermal reservoir for solar steam generation in absence of bulk water due to its remarkable photothermal property, excellent wettability and high water absorbency. Evaporation rate over the carbon aerogel saturated with water was 3.5 times higher than the bare water system under one sun irradiation. Moreover, the carbon aerogel showed high performance in adsorption of MB with the theoretical maximum capacity of 108 mg g^{-1}. Also, it can be used as a self-floating absorbent for the removal of MB from water, and the adsorption kinetics can be described by pseudo-second-order kinetics model.

ACKNOWLEDGEMENT

The author wishes to thank the anonymous reviewers for their useful comments.

FUNDING

This work was financially supported by National Natural Science Foundation of China (51909292) and Fundamental Research Funds for Central Public Welfare Scientific Research Institution (K-JBYWF-2021-ZT04).

REFERENCES

1. Y. Liu, T. Shi, T. Zhang, D. Yuan, Y. Peng and F. Qiu, *Cellulose*, **26**, 5381 (2019).
2. S. Long, Y. Feng, F. He, S. He, H. Hong, X. Yang, L. Zheng, J. Liu, L. Gan and M. Long, *Carbon*, **158**, 137 (2020).
3. H. Zhuo, Y. Hu, Z. Chen, X. Peng, H. Lai, L. Liu, Q. Liu, C. Liu and L. Zhong, *ACS Appl. Mater. Interfaces*, **8**, 11921 (2020).
4. H. Wang, A. Du, X. Ji, C. Zhang, B. Zhou, Z. Zhang and J. Shen, *ACS Appl. Mater. Interfaces*, **11**, 42057 (2019).
5. L. Li, T. Hu, A. Li and J. Zhang, *ACS Appl. Mater, Interfaces*, **12**, 32143 (2020).
6. Z. Huang, Y. Wan, J. Liang, Y. Xiao, X. Li, X. Cui, S. Tian, Q. Zhao, S. Li and C. S. Lee, *ACS Appl. Mater. Interfaces*, **13**, 31624 (2021).
7. P. Mu, Z. Zhang, W. Bai, J. He, H. Sun, Z. Zhu, W. Liang and A. Li, *Adv. Energy Mate.*, **9**, 1802158 (2019).
8. C. Chen, Y. Kuang and L. Hu, *Joule*, **3**, 683 (2019).
9. P. Wang, *Environ. Sci.: Nano*, **5**, 1078 (2018).
10. Y. Fu, G. Wang, T. Mei, J. Li, J. Wang and X. Wang, *ACS Sustain. Chem. Eng.*, **5**, 4665 (2017).
11. X. Deng, Q. Nie, Y. Wu, H. Fang, P. Zhang and Y. Xie, *ACS Appl. Mater. Interfaces*, **12**, 26200 (2020).
12. S. Zhai, R. Chen, J. Liu, J. Xu and H. Jiang, *J. Taiwan Inst. Chem. E*, **120**, 161 (2021).
13. X. Jiang, X. Xiang, S. Peng and L. Hou, *Cellulose*, **26**, 4515 (2019).
14. C. Wang, S. Yang, Q. Ma, X. Jia and P.-C. Ma, *Carbon*, **118**, 765 (2017).
15. M. Zhang, B. Gao, X. Cao and L. Yang, *RSC Adv.*, **3**, 21099 (2013).
16. S.-J. Yuan, J.-J. Zhang, H.-X. Fan and X.-H. Dai, *J. Clean. Prod.*, **196**, 644 (2018).
17. H. Xu, L. Huang, M. Xu, M. Qi, T. Yi, Q. Mo, H. Zhao, C. Huang, S. Wang and Y. Liu, *ACS Omega*, **5**, 23743 (2020).
18. F. Sotoudehnia, A. Baba Rabiu, A. Alayat and A. G. McDonald, *J. Anal. Appl. Pyrol.*, **145**, 104722 (2020).
19. Y. Liu, C. Yan, Z. Zhang, Y. Gong, H. Wang and X. Qiu, *Mater. Lett.*, **185**, 370 (2016).
20. D. Tian, Z. Xu, D. Zhang, W. Chen, J. Cai, H. Deng, Z. Sun and Y. Zhou, *J. Solid State Chem.*, **269**, 580 (2019).
21. M. A. Islam, S. Sabar, A. Benhouria, W. A. Khanday, M. Asif and B. H. Hameed, *J. Taiwan Inst. Chem. E*, **74**, 96 (2017).

22. Y. Wang, Y. Feng, X. F. Zhang, X. Zhang, J. Jiang and J. Yao, *J. Colloid Interface Sci.*, **514**, 190 (2018).
23. Y. An, H. Zheng, Z. Yu, Y. Sun, Y. Wang, C. Zhao and W. Ding, *J. Hazard. Mater.*, **381**, 120971 (2020).
24. I. Mian, X. Li, Y. Jian, O. D. Dacres, M. Zhong, J. Liu, F. Ma and N. Rahman, *Bioresour. Technol.*, **294**, 122099 (2019).
25. G. Ganeshan, K. P. Shadangi and K. Mohanty, *J. Therm. Anal. Calorim.*, **131**, 1803 (2017).
26. Y. J. Rueda-Ordonez and K. Tannous, *Bioresour. Technol.*, **196**, 136 (2015).
27. G. Mishra and T. Bhaskar, *Bioresour. Technol.*, **169**, 614 (2014).
28. L. Zhang, K. Li and X. Zhu, *J. Anal. Appl. Pyrol.*, **127**, 91 (2017).
29. M. Liu, J. Li and Y. Duan, *Energy Convers. Manage.*, **103**, 66 (2015).
30. W. Chen, S. Shi, J. Zhang, M. Chen and X. Zhou, *Energy Convers. Manage.*, **112**, 41 (2016).
31. W.-L. Wang, X.-Y. Ren, L.-F. Li, J.-M. Chang, L.-P. Cai and J. Geng, *Fuel Process Technol.*, **134**, 345 (2015).
32. X. Yang, Z. Fu, D. Han, Y. Zhao, R. Li and Y. Wu, *Renew. Energy*, **147**, 1120 (2020).
33. P. Halder, S. Kundu, S. Patel, R. Parthasarathy, B. Pramanik, J. Paz-Ferreiro and K. Shah, *Energy Convers. Manage.*, **200**, 112067 (2019).
34. X. Yang, Y. Zhao, R. Li, Y. Wu and M. Yang, *Thermochim. Acta*, **665**, 20 (2018).
35. C. Qi, C. Luo, Y. Tao, W. Lv, C. Zhang, Y. Deng, H. Li, J. Han, G. Ling and Q.-H. Yang, *Sci. China Mater.*, **63**, 1870 (2019).
36. S. K. Singh, T. G. Townsend, D. Mazyck and T. H. Boyer, *Water Res.*, **46**, 491 (2012).
37. Y. Jeong, M. Cui, J. Choi, Y. Lee, J. Kim, Y. Son and J. Khim, *Chemosphere*, **238**, 124559 (2020).
38. M. Mohsenpour, S. Motahari, F. Tajabadi and M. Najafi, *RSC Adv.*, **10**, 41780 (2020).
39. P. Liu, L. Wang, Y. Zhou, T. Pan, X. Lu and D. Zhang, *Fuel*, **164**, 110 (2016).
40. S. Wang, H. Lin, B. Ru, W. Sun, Y. Wang and Z. Luo, *J. Anal. Appl. Pyrol.*, **108**, 78 (2014).
41. C. Song, B. Zhang, L. Hao, J. Min, N. Liu, R. Niu, J. Gong and T. Tang, *Green Energy Environ.*, **7**, 411 (2022).
42. B. Y. Jibril, R. S. Al-Maamari, G. Hegde, N. Al-Mandhary and O. Houache, *J. Anal. Appl. Pyrol.*, **80**, 277 (2007).
43. Y. Bai, P. Wang, L. Yan, C. Liu, F. Li and K. Xie, *J. Anal. Appl. Pyrol.*, **104**, 202 (2013).
44. S. Secchi, F. Asdrubali, G. Cellai, E. Nannipieri, A. Rotili and I. Vannucchi, *J. Build. Eng.*, **5**, 1 (2016).
45. X. Qi, X. Guo, L. Xue and C. Zheng, *J. Anal. Appl. Pyrol.*, **110**, 401 (2014).
46. J. Yan, W. Xiao, L. Chen, Z. Wu, J. Gao and H. Xue, *Desalination*, **516**, 115224 (2021).
47. L. Sun, J. Liu, Y. Zhao, J. Xu and Y. Li, *Carbon*, **145**, 352 (2019).
48. S. Ma, W. Qarony, M. I. Hossain, C. T. Yip and Y. H. Tsang, *Sol. Energ. Mater. Sol. C*, **196**, 36 (2019).
49. W. Sun, A. Du, Y. Feng, J. Shen, S. Huang, J. Tang and B. Zhou, *ACS Nano*, **10**, 9123 (2016).
50. H. Bi, X. Huang, X. Wu, X. Cao, C. Tan, Z. Yin, X. Lu, L. Sun and H. Zhang, *Small*, **10**, 3544 (2014).
51. Y. Meng, T. M. Young, P. Liu, C. I. Contescu, B. Huang and S. Wang, *Cellulose*, **22**, 435 (2014).
52. W. Yuan, C. Hou, X. Zhang, S. Zhong, Z. Luo, D. Mo, Y. Zhang and X. Liu *ACS Appl. Mater. Inter.*, **11**, 37626 (2019).
53. S. J. Bao, C. X. Guo and C. M. Li, *RSC Adv.*, **2**, 1014 (2012).
54. H. Bi, Z. Yin, X. Cao, X. Xie, C. Tan, X. Huang, B. Chen, F. Chen, Q. Yang, X. Bu, X. Lu, L. Sun and H. Zhang, *Adv. Mater.*, **25**, 5916 (2013).
55. S. Kabiri, D. N. H. Tran, T. Altalhi and D. Losic, *Carbon*, **80**, 523 (2014).
56. Z. Miao, H. Yu, W. Song, D. Zhao, L. Hao, B. Yi and Z. Shao, *Electrochem. Commun.*, **11**, 787 (2009).
57. F. Ardeshiri, A. Akbari, M. Peyravi and M. Jahanshahi, *Korean J. Chem. Eng.*, **36**, 255 (2018).
58. J. Cui, Z. Zhou, A. Xie, M. Meng, Y. Cui, S. Liu, J. Lu, S. Zhou, Y. Yan and H. Dong, *Sep. Purif. Technol.*, **209**, 434 (2019).
59. B. Yuan, C. Zhang, Y. Liang, L. Yang, H. Yang, L. Bai, D. Wei, W. Wang, Q. Wang and H. Chen, *Adv. Sustain. Syst.*, **5**, 2000245 (2020).
60. C. F. Wang, C. L. Wu, S. W. Kuo, W. S. Hung, K. J. Lee, H. C. Tsai, C. J. Chang and J. Y. Lai *Sci. Rep.-UK*, **10**, 12769 (2020).
61. H. Qiao, B. Zhao, X. Suo, X. Xie, L. Dang, J. Yang and B. Zhang, *Glob. Chall.*, **6**, 2100083 (2021).
62. J. Fang, J. Liu, J. Gu, Q. Liu, W. Zhang, H. Su and D. Zhang, *Chem. Mater.*, **30**, 6217 (2018).
63. X. Zhou, J. Li, C. Liu, F. Wang, H. Chen, C. Zhao, H. Sun and Z. Zhu, *Int. J. Energ. Res.*, **44**, 9213 (2020).
64. Y. Long, S. Huang, H. Yi, J. Chen, J. Wu, Q. Liao, H. Liang, H. Cui, S. Ruan and Y.-J. Zeng, *J. Mater. Chem. A*, **7**, 26911 (2019).
65. N. Xu, X. Hu, W. Xu, X. Li, L. Zhou, S. Zhu and J. Zhu, *Adv. Mater.*, **29**, 1606762 (2017).